Preprint Title Greatly improved adsorption and degradation by S-doped (001)-TiO_2 via the vapour-thermal method

Authors X. Y. Sun, X. Zhang, X. Sun, N. X. Qian, Min Wang and Y. Q. Ma

Article Type Full Research Paper

ORCID® iDs Y. Q. Ma - https://orcid.org/0000-0001-5485-2151

Greatly improved adsorption and degradation by S-doped (001)-TiO_2 via the vapour-thermal method

X.Y. Sun[2], X. Zhang[2,3], X. Sun[2], N.X. Qian[2], M. Wang[2,*], Y.Q. Ma[1,2,*]

[1]*Institute of Physical Science and Information Technology, Anhui University, Hefei 230039, China*

[2]*Anhui Key Laboratory of Information Materials and Devices, School of Physics and Materials Science, Anhui University, Hefei 230039, China*

[3] *School of Electronic Engineering, Huainan Normal University, Huainan 232038, China*

Abstract

In this work, sulfur (S) doped (001)-face exposed TiO_2 was synthesized via the vapor-thermal method at 180 °C or 250 °C, with an S/Ti molar ratio $R_{S/Ti}$ of 0, 0.5, 1, 2, 3, 4, and 5. The S-doped samples at 250 °C exhibited significantly improved photocatalytic performance. The effects of S doping were as follows: (1) The S element exhibits different chemical states in the samples with different $R_{S/Ti}$. Specifically, it exists in the form of S^{2-} replacing O^{2-} at $R_{S/Ti}$ = 1, and S^{6+} replacing Ti^{4+} at $R_{S/Ti} \geq 2$. As a result, S doping causes a lattice distortion because the ionic radii of S^{2-} and S^{6+} differ from that of the O^{2-} and Ti^{4+}. (2) S-doping increases the adsorption coefficient A_e for methylene blue (MB) from 0.9% to 68.5% due to the synergistic effects of the oxygen vacancies, the SO_4^{2-} adsorbed on the TiO_2 surface, and the pore size. (3) S-doping increases the MB degradation rate from 6.9×10^{-2} min^{-1} to 18.2×10^{-2} min^{-1} due to an increase in the amount of •OH and $•O^{2-}$ radicals.

Keywords: Vapour-thermal; S-doping; TiO_2; photocatalytic properties; chemical state

*Corresponding author. M. Wang, E-mail: ahwm@ahu.edu.cn; Y.Q. Ma, *E-mail:* yqma@ahu.edu.cn (Y.Q. Ma).

1. Introduction

Anatase TiO_2 with a tetragonal symmetry has been widely used for the degradation of organic pollutants, electrocatalysis, solar cells, and self-cleaning. Its wide use stems from favorable attributes such as its stable physicochemical properties, abundant reserve, nontoxicity, environment-friendliness, and low cost. [1-7] The photocatalytic properties of anatase TiO_2 crystals are anisotropic since the different exposed crystal faces have different atomic and electronic structures and surface energy. This results in differences in the adsorption capacity of the pollutant molecules by TiO_2 and the electron transfer properties. For examples, Ti atoms with an exposed (001) anatase face are 100% 5-coordinated Ti atoms (Ti_{5c}); half the exposed Ti atoms on the (101) face are Ti_{5c} atoms. This results in significant differences in the adsorption capacity between the (001) and (101) faces. Previous work using first-principles simulations showed that holes easily migrate to the {001} faces and electrons easily migrate to the {101} faces; therefore, the oxidation and reduction reactions preferentially occur on the {001} and {101} faces, respectively. [8-9] In addition, the results of theoretical calculations show that the surface energy varies between the different crystal faces in anatase TiO_2 in the order: (110) (1.09 J m^{-2}) > (001) (0.90 J m^{-2}) > (010) (0.53 J m^{-2}) > (101) (0.44 J m^{-2}). [5] It was widely believed that the exposed (001) face has a high photocatalytic activity; however, Yu et al. [8] demonstrated that an appropriate proportion of exposed (001) and (101) crystal faces, which forms a "surface heterojunction", facilitates the separation of photo-generated carriers. Consequently, this improves the photocatalytic performance. Wang et al. reported that TiO_2 with the ideal (001) face was very inert to both methanol and water, and the activity of the (001) face was only enhanced after surface reduction or reoxidation. [10]

It is well-known that the conduction band of anatase TiO_2 is composed of the Ti 3d state and the valence band mainly comprises the O 2p states, with a band gap energy (E_g) of 3.2 eV. Therefore, the photo-excitation of electron-hole pairs requires photon energies $h\nu \geq 3.2$ eV (wavelength $\lambda < 387$ nm); this means that the photo-response

range of TiO_2 lies in the ultraviolet region and it can only harness < 5% of the total energy of the solar spectrum. [11] Therefore, increasing the spectral response range of TiO_2 has become an important research area.

Significant efforts have been devoted to the post-treatment of the (001) face exposed TiO_2 [denoted as (001)-TiO_2] to further improve its photocatalytic performance. Li et al. synthesized composites of mesoporous (001)-TiO_2 and C via a one-pot hydrothermal strategy in the presence of glucose and hydrofluoric acid (HF). The composite exhibited excellent visible-light-driven photocatalytic performance. [12] Chen et al. synthesized a composite of g-C_3N_4 and B-doped (001)-TiO_2 via the solvothermal method in order to improve the visible-light photocatalytic activity. [13] Cao et al. used first-principles simulations to study the electronic and optical properties of (001)-TiO_2 and MoS_2 composites. Their results suggested that the effective photosensitization of MoS_2 and the stable interface between the two phases could promote the transfer of electrons from MoS_2 to (001)-TiO_2 and enhance its visible-light response. [14] It was also demonstrated that Au nanoparticles deposited on the surface of (001)-TiO_2 particles could promote the separation of photo-generated carriers, improve cycle stability, and enhance the visible light response. [15-16]

In addition to the composite two-phase approach described above, several groups reported elemental substitution in (001)-TiO_2, with the aim of improving its photocatalytic performance. For example, a theoretical study on C/F co-doped (001)-TiO_2 concluded that C/F atoms preferentially replaced O atoms on the (001) face, resulting in a surface conduction layer that could promote the migration of photo-generated carriers. [17] N/P co-doping of (001)-TiO_2 resulted in a reduction of the band gap from 3.20 eV to 2.48 eV. [18] To the best of our knowledge, S-doped (001)-TiO_2 has not yet been reported in literature.

The current literature on S-doped non-(001)-TiO_2 are summarized as follows. (1) Ti-containing carbides, nitrides, and sulfides were annealed in air at 350–650 °C to synthesize C, N, and S-doped TiO_2, respectively. [11] Their UV–Vis spectra exhibited a “shoulder” or “tail-like” absorption in the visible light region. The results of the valence band XPS measurements showed that C and N doping induced multiple

energy levels, while S doping induced diffusive states above the valence band maximum. The electron transition from the impurity states to the Ti 3d state gives rise to a "shoulder" or "tail-like" absorption in the visible light region. (2) S-doped TiO_2 thin films were synthesized via the sol-gel method with subsequent calcination at different temperatures; [19] The morphological and porous structure of the material was sensitive to the calcination temperatures and calcination at 350 °C could improve the adsorption of pollutants. The S doping introduces a localized state in the TiO_2 band gap. The undoped sample could not degrade hepatotoxin microcystin-LR (MC-LR), while the degradation efficiency for the doped sample reached 33% under visible light irradiation for 5 hours. (3) The S doped in TiO_2 exists in the form of S^{4+} or S^{6+}. [20-22] (4) Ramacharyulu et al. synthesized S-doped TiO_2 via the sol-gel and hydrothermal methods. [23] It was observed that S^{4+}/S^{6+} replaced Ti ions in the TiO_2 lattice and produced a hybrid state near the conduction band. This narrowed the band gap and enhanced the visible light response of TiO_2. The S-doped sample could degrade toxic sulphur mustard completely within 120 minutes under sunlight. (5) Colon et al. prepared sulfated TiO_2 powders by immersion and subsequent calcination. [24] It was determined that S^{6+}/S^{4+} exists in the form of sulfate (SO_4^{2-}/SO_3^{2-}) that is coordinated to the surface of the TiO_2 particles through the Ti^{4+} ions. The presence of SO_4^{2-}/SO_3^{2-} stabilized the anatase phase, and the sulfate surface caused the formation of oxygen vacancies during calcination, which could promote the photocatalytic effect. The presence of different forms of S^{4+}/S^{6+} mainly depends on the synthesis conditions or the type of the sulfur precursor. [19] In summary, S-doping in previous reports was mainly performed via the solid-state calcination or hydrothermal methods. Solid-state calcination results in the aggregation of particles. For S-doping carried out via the hydrothermal method in an autoclave, the precursors were placed in an oven or a muffle furnace and heated to carry out the reaction.

While much progress has been made on S-doped TiO_2, there are many issues that require further investigation. These include the differences between lightly- and heavily-doped TiO_2, the effects of S-doping on the crystal structure, energy band structure, and the chemical states of Ti and O. In this work, (001)-TiO_2 nanoparticles

were prepared first, then S-doping was performed via the vapour-thermal method. It was observed that S-doping greatly enhanced the photocatalytic performance of (001)-TiO_2, and the related mechanism was revealed by a systematic investigation.

2. Experimental procedure

2.1 Synthesis of nanoparticles

20 mL of tetrabutyl titanate (TBT, 99%, Aladdin) was added into a Teflon-lined stainless steel autoclave. Then, 5 mL of deionized water and 5 mL of a HF acid solution (Hydrofluoric acid, 40%, Aladdin) were added sequentially. The autoclave was maintained at 180 °C for 8 hours and then then cooled naturally to room temperature. The obtained precipitate was washed several times with deionized water and absolute ethanol, respectively, and then dried at 60 °C to obtain the resulting (001)-TiO_2 nanoparticles (NPs).

S-doping of the (001)-TiO_2 was performed via the vapour-thermal method. First, 300 mg of (001)-TiO_2 NPs was added to a beaker containing 100 mL deionized water. Then, the desired amount of thiourea (99%, Aladdin) was added; the molar ratio of S in the thiourea to Ti in TiO_2 ($R_{S/Ti}$) was 0, 0.5, 1, 2, 3, 4, and 5. After magnetic stirring for 30 min, the solution was transferred to a 120 mL quartz-goblet, which was subsequently placed inside a 500 mL Hastelloy autoclave and 150 mL of deionized water was added to the autoclave. The autoclave was then heated to 180 °C or 250 °C, and maintained at temperature for 12 hours. The reaction occurred in the quartz-goblet under the high-temperature vapour environment of deionized water. Such a vapour-thermal reaction has the advantages of rapid heat transfer, uniform heating, and accelerating the diffusion of S atoms in the TiO_2 crystal lattice. After the autoclave cooled naturally to room temperature, the precipitate was washed several times with deionized water and absolute ethanol, respectively, and then dried at 60 °C. The S-doped TiO_2 samples were synthesized at 180 °C and named as 1-S0, 1-S0.5, 1-S1, 1-S2, 1-S3, 1-S4, and 1-S5; samples synthesized at 250 °C were named

as 2-S0, 2-S0.5, 2-S1, 2-S2, 2-S3, 2-S4, and 2-S5.

2.2 Characterization

The crystal structure of the samples was investigated via X-ray diffraction (XRD) using an X-ray diffractometer (XRD, Rigaku Industrial Corporation, Osaka, Japan) with Cu Kα radiation (λ = 1.5406 Å) (operated at 40 kV and 100 mA). Transmission electron microscopy (TEM; JEM-2100, JEOL, Tokyo, Japan) was used to observe the morphology. The ultraviolet visible diffuse reflectance spectra (UV-Vis DRS) of the samples were measured on a Shimadazu U-4100 spectrometer (U-4100, Shimadazu Corporation, Tokyo, Japan). X-ray photoelectron spectroscopy (XPS) was performed on a Thermo Scientific ESCALAB 250Xi (Thermo Scientific Inc., USA). The chemical bonds of the photocatalysts were probed via Fourier transform infrared (FT-IR) spectroscopy (Vertex 80/Hyperion2000, Bruker, Germany). The Brunauer–Emmett–Teller (BET) specific surface areas were calculated based on the N_2 adsorption-desorption isotherms measured at 77 K using a gas adsorption apparatus (Autosorb-iQ, Quantachrome Instruments, USA). The pore size distribution was calculated by the BJH method. The photoluminescence (PL) was measured on a FL fluorescence spectrophotometer (F-4500 , Hitachi , Japan). Electron spin resonance (ESR) signals of the reactive species spin trapped by 5,5-dimethyl-L-pyrroline-N-oxide (DMPO) were determined on a Bruker EMX plus 10/12 (equipped with Oxford ESR910 Liquid Helium cryostat). For detection of the superoxide radicals ($\bullet O_2^-$) and hydroxyl radicals (•OH), 2.5 mg of the photocatalyst was dispersed in 1 mL DMPO/methyl alcohol solution or DMPO/H_2O solution, respectively.

The photocatalytic activity was tested by the degradation of methylene blue. For this, the samples were placed 20 cm away from a xenon lamp (300 W, 16 A). The experimental process was as follows: 50 mg of catalyst was added into a 100 mL methylene blue solution with a concentration of 10 mg/L, and the samples were kept in a dark room for 30 min to achieve the adsorption–desorption equilibrium. After

light irradiation, samples of the solution were taken every 10 min. After high-speed centrifugation, the concentration of methylene blue was analyzed by a UV–Vis spectrometer (UV-3200S, MAPADA, Shanghai, China) and calculated using a calibration curve.

3. Results and Discussion

The crystal structures of all the samples were characterized by XRD. Fig. 1 shows the experimental data and the results calculated by Rietveld refinement of 1-S0 (a) and 2-S2 (b). The calculated results match well with the experimental data, indicating that all the TiO_2 samples have a single-phase anatase structure with tetragonal symmetry and the space group I41/AMD. The unit cell parameters of the un-doped samples 1-S0 were a = 3.7852 Å and c = 9.5139 Å; there was minimal change for the S-doped samples at 180 ℃; however, there was an observed change in the $R_{S/Ti}$ for samples synthesized at 250 °C, as shown in Table 1; this was due to the S element entering the lattice. The value of c/a gradually increased from 2-S0.5 to 2-S3 and reached a maximum for the 2-S3 sample, and then decreased. The reason for the variation of c/a with $R_{S/Ti}$ will be discussed in detail in section XPS.

Fig. 2 shows the TEM and HTEM images of the 1-S0 (a, d), 2-S0 (b, e), and 2-S2 (c, f) samples. It can be seen that the undoped 1-S0 sample synthesized at 180 ℃ was composed of square sheet-like particles, which is the typical morphology of (001)-TiO_2. [8,25,26] The HRTEM image (Fig. 2d) of the particle side shows a lattice fringes spacing of 0.238 nm. This corresponds to the (004) crystal face of TiO_2 and indicates that the top and bottom square surfaces (pointed by the arrow) are the (001) faces. [27] For samples synthesized at 250 °C, the TEM images (Figs. 2b and 2c) of the undoped 2-S0 and S-doped 2-S2 show that the edges and corners of some of the square particles become blurred. The HRTEM images (Figs. 2e and 2f) of the particle sides also exhibit lattice fringes associated with the (004) crystal face.

FT-IR spectra were measured for all the samples. Fig. 3 shows the results of the samples with $R_{S/Ti}$ = 0, 2, and 5. The wavenumbers and vibration modes that

correspond to the absorption peaks are listed in Table 2. Compared to the undoped 1-S0 and 2-S0 samples, all the S-doped samples exhibit the Ti-S vibration mode with an absorption peak located at 1060 cm^{-1}. Compared with the S-doped samples at 180 °C (Fig. 3a), the S-doped samples at 250 °C (Fig. 3b) exhibit the following differences: (1) the Ti-S vibration is stronger. (2) A new vibration mode appears, i.e., the Ti-O-S vibration at 1160 cm^{-1} [19] caused by S^{6+} replacing Ti^{4+} (this was also confirmed by the following XPS results). (3) The S=O vibration in the range of 1380 cm^{-1}–1400 cm^{-1} results from the sulfate complex formed by the surface-adsorbed SO_4^{2-} group and the TiO_2 [29]. (4) The vibration modes at 1800 cm^{-1} and 2515 cm^{-1} can be attributed to the -COOH vibration [30,31]; while those at 2850 cm^{-1} and 2920 cm^{-1} can be attributed to the C-H vibration[34]; the C-OH vibration mode is located at 880 cm^{-1} [32,33]. (5) The vibration mode at 2138 cm^{-1} can be attributed to the C-N vibration, which results from the residue after thiourea decomposition. [35,36]

In order to investigate the variation of the elemental chemical states (CS) of the S-doped (001)-TiO_2 with the $R_{S/Ti}$, the core energy level XPS spectra of the Ti 2p, O 1s, and S 2p regions were measured for samples 1-S0, 1-S2, and 1-S5. Fig. 4 representatively shows the results of 1-S2. The S element was not detected by XPS for the three samples; this could be due to the small amount of S atoms doped in the samples or adsorbed on the TiO_2 surface. [41] The XPS spectrum of Ti 2p can be fitted by two peaks and the CSs correspond to TiO_2 and TiO_x. [42,43] The XPS spectrum of O 1s can be fitted by two peaks as well and the CSs correspond to TiO_2 and -OH. [44,45] The CS of the Ti and O elements, their corresponding binding energies (BE), and the ratios for 1-S0, 1-S2, and 1-S5 are listed in Table 3. It can be seen that the CS ratios for Ti and O in TiO_2 do not change significantly with $R_{S/Ti}$ when S doping is carried out at 180 ℃.

The core energy level XPS spectra of the Ti 2p, O 1s, and S 2p regions for all the S-doped samples synthesized at 250 °C were measured, and Fig. 5 representatively shows the results for 2-S1 and 2-S3. The chemical states of the Ti, O, and S elements, their corresponding BE, and the ratios for 2-S0, 2-S0.5, 2-S1, 2-S2, 2-S3, 2-S4, and 2-S5 are listed in Table 4.

The XPS spectrum of O 1s can be fitted by three peaks and the CSs correspond to TiO_2, -OH, and O_v. [46] As the $R_{S/Ti}$ increases, the ratio of O_v increases from 4.3% (2-S0) to 22.9% (2-S3) and then decreases to 19.9% (2-S5). The XPS signals of the oxygen vacancies were not detected in the S-doped samples at 180 ℃, but they appear in the S-doped samples at 250 ℃ due to the reducibility of thiourea [47] and the influence of the S-doped element.

The XPS signal of the S element was not detected in the S-doped samples at 180 °C. For the S-doped samples at 250 °C, the XPS spectrum of the S 2p region can be fitted by three peaks, the CSs correspond to Ti-S, S^0, and S^{6+}. [19,48] The substitution of S^{2-} for O^{2-} in the TiO_2 lattice is responsible for the formation of the Ti-S bond. [19] The neutral S (S^0) comes from the hydrolysis of thiourea at high temperature, [49] which is believed to adsorb on the TiO_2 surface or partially enter the interstitial sites of the TiO_2 lattice. Some of the S^{6+} ions replace the Ti^{4+} ions in the TiO_2 crystal lattice, while others exist in the SO_4^{2-} groups. [50]

From Table 4, it can be seen that the XPS signal of the S element in 2-S0 and 2-S0.5 cannot be detected. For the 2-S1 sample, S replaces O to form the Ti-S bond, which is accompanied by the appearance of S^0. For the 2-S2 sample, apart from the chemical states of Ti-S and S^0, S^{6+} appears which replaces Ti^{4+}. For the samples with $R_{S/Ti} \geq 2$, as $R_{S/Ti}$ increase, the proportion of S^{6+} replacing the Ti^{4+} decreases, while the sum of S^{2-} and S^0 increases. The ionic radii of S^{6+} and S^{2-} are 0.029 nm and 0.17 nm, respectively, while the ionic radii of Ti^{4+} and O^{2-} in the TiO_2 lattice are 0.064 nm and 0.122 nm, respectively. As a result, the substitution of S^{6+} for Ti^{4+} or S^{2-} for O^{2-} consequentially induces a lattice distortion. [41] The lattice distortion degree (ΔR) is calculated according to $\Delta R = r_{S6+} (R_{Ti4+} - R_{S6+}) + r_{S2-} (R_{S2-} - R_{O2-})$, where r is the ratio of the CSs and R is the ionic radius and ΔR is 0.024 nm (2-S1), 0.032 nm (2-S2), 0.034 nm (2-S3), 0.028 nm (2-S4), and 0.028 nm (2-S5), respectively. The 2-S3 sample has the largest ΔR, which is consistent with the XRD results.

The XPS spectra can not only provide information on the binding energy of elements but also about the total density of states (DOS) in the valence band of the TiO_2. [11,51] In order to observe whether S doping produces energy levels above the

valence band maximum, we measured the valence-band XPS spectra of the 2-S0, 2-S0.5, 2-S1, 2-S3, and 2-S5 samples, as shown in Fig. 6(a). The valence band maximum for all the samples was located around 2.4 eV, so S-doping does not shift the valence band maximum towards the forbidden band. The mid-gap states or diffusive states observed in C, N, and S-doped TiO_2 caused by impurities [11] were not observed in our samples. A peak around 7.1 eV was observed in the valence band DOS curve, and its intensity is in the order of 2-S0.5 > 2-S1 > 2-S5 > 2-S3. The states in the valence band are derived from the O 2p orbitals. As listed in Table 4, the ratio of the oxygen vacancies for the S doped samples changes in order 2-S0.5 < 2-S1 < 2-S5 < 2-S3; therefore, the decrease in the DOS mainly results from an increase in the oxygen vacancies.

Fig. 6(b) shows the UV-Vis DRS of 2-S0, 2-S0.5, 2-S1, 2-S3, and 2-S5. The steep absorption edge near 380 nm originates from the intrinsic absorption of TiO_2, i.e., the absorption results from the transition of electrons from the valence band to the conduction band. The undoped 2-S0 sample exhibits a "tail-like" absorption between 400 nm and 500 nm, possibly due to surface defects, such as oxygen vacancies. The absorption spectra of the 2-S0.5 sample shows a peak at 460 nm. The visible-light absorption of the samples with $R_{S/Ti} \geq 1$, where S^{2-} replaces O^{2-} and S^{6+} replaces Ti^{4+}, is caused by the cooperative effects of the oxygen vacancies and the substituted S elements.

The photocatalytic degradation abilities of samples 1-S0–1-S5 (a) and 2-S0–2-S5 (b) were tested with methylene blue (MB) as the target pollutant, and the results are shown in Fig. 7. The negative time denotes the adsorption process of MB in the dark, and the positive one denotes the photodegradation process of MB under light irradiation. The concentration of MB at t = - 30 min is referred to as the initial concentration C_0. After 30 min of adsorption, the concentration decreases to C_e at t = 0. The adsorption efficiency (A_e), calculated by (C_0 - C_e) / C_0. The degradation efficiency (D_e) is calculated by (C_e - C) / C_e, where C is the concentration at an irradiation time t. The degradation process can be fitted using a pseudo first-order

kinetic model $ln[C_e / C] = K_{app}t$, where K_{app} is the apparent reaction rate constant. The A_e, D_e, and K_{app} for all samples are listed in Table 5 and Table 6.

It can be seen From Table 5 that samples1-S0 to 1-S5 hardly adsorb any MB, and the adsorption coefficients range from 0–5.7%. However, the adsorption coefficients for samples 2-S0.5 to 2-S5 are significantly enhanced, ranging from 0.9–68.5%. Generally, the larger the specific surface area of the sample, the stronger the adsorption capacity; however, the results of the BET surface areas (S_{BET}) in Table 7 show that the specific surface area of samples 2-S0.5 to 2-S5 is less than that of samples 1-S0 to 1-S5. Microscopically, the adsorption capacity of TiO_2 to water or organic pollutant molecules is determined by the amount and distance of oxygen vacancies (or Ti^{3+}) on the surface of the TiO_2 particles. [52] The adsorption coefficient (A_e) and oxygen vacancies ratio of 2-S0.5 to 2-S5 change with $R_{S/Ti}$ with an almost similar trend. This indicates that the adsorption is mainly determined by the oxygen vacancies. Additionally, the SO_4^{2-} group adsorbed on the surface of the S-doped samples at 250 °C produces acidic sites on the TiO_2 surface. [29,53] These acidic sites provide more surface chemical adsorption centers for reactants and oxygen molecules, thus, enhancing the adsorption effect.

The S-doped samples at 180 °C are able to degrade MB within 120 min, and the degradation coefficients vary from 92.5% to 99.8%; however, for the S-doped samples at 250 °C, the MB is almost completely degraded within 80 min, and the degradation coefficients (D_e) exceed 99.4%.

For the samples synthesized at 180 ℃, the K_{app} of the undoped 1-S0 sample was 1.7×10^{-2} min^{-1}; after S-doping, the K_{app} of the 1-S4 sample was the largest and reached 3.67×10^{-2} min^{-1}, which was 2.16 times higher than that of 1-S0. For the samples synthesized at 250 ℃, the K_{app} of the undoped 2-S0 sample was 6.94×10^{-2} min^{-1}; after S-doping, the K_{app} of the 2-S2 was the largest and reached 18.2×10^{-2} min^{-1}, which was 2.62 times higher than that of 2-S0. In contrast, the degradation performance of the commercial P25 TiO_2 to MB was also tested by the same method; the K_{app} value was determined to be 7.5×10^{-2} min^{-1}, which was much smaller than that of 2-S2.

The S_{BET} of all the samples were investigated by nitrogen adsorption-desorption isotherms. Fig. 8 shows the results for samples 1-S0, 1-S2, and 1-S5 (a) and for 2-S0, 2-S2, and 2-S5 (b). The Barret–Joyner–Halenda (BJH) desorption pore distribution (D_p) analysis results are shown in the insets of Figs. 8(a) and 8(b). The S_{BET} and D_p values for all the samples are listed in Table 7. The S_{BET} of almost all the S-doped samples at 250 °C was reduced, compared to the S-doped samples at 180 °C. This can be mainly ascribed to the agglomeration of TiO_2 particles synthesized at 250 °C, as shown by the TEM results. In addition, the S-doped samples at 250 °C had a larger pore size, which was beneficial for adsorption of the pollutant molecules.

Fig. 9 shows the photoluminescence spectra of samples 1-S0, 1-S0.5, 1-S2, 1-S3, and 1-S5 (a), and 2-S0, 2-S0.5, 2-S2, 2-S3, and 2-S5 (b). Photoluminescence is an effective way to survey the separation efficiency and recombination processes of photo-generated carriers. This is because increased photo-generated electron-hole pair recombination results in a stronger luminescence intensity. The positions of the emission peaks for all the samples were at 421 nm, 474 nm, and 541 nm and were almost unchanged. The emission peak at 421 nm results from the interband transition of TiO_2. The emission peaks at 474 nm and 541 nm can be attributed to the radiative recombination processes of the self-trapped excitons and the hydroxylated Ti^{3+} surface complexes, respectively. [54,55] As the $R_{S/Ti}$ increases, there was no obvious trend in the change of the luminescence intensity of the S-doped samples at 180 ℃. However, for the S-doped samples at 250 ℃, the luminescence intensity increases initially, with the 2-S2 sample having the strongest luminous intensity. Then, the luminescence intensity decreases with sample 2-S5 having the weakest intensity. It can be seen from the XPS results that there are various impurities and defects in the S-doped TiO_2, such as O_v (Ti^{3+}), -OH, and S impurities; furthermore, the change of their proportion is the most likely reason for the change in the luminescence intensity.

Fig. 10 shows the ESR spectra for samples 2-S0 (a, e), 2-S2 (b, f), 2-S3 (c, g), and 2-S5 (d, h). Before light irradiation, there was no obvious signal in the ESP spectra. After light irradiation, the superoxide radical ($\bullet O_2^-$) and hydroxyl radical (•OH) signals clearly appear in all the samples. TiO_2 is excited by photons to generate

electron-hole pairs, i.e., $TiO_2 + h\nu = TiO_2 + e^- + h^+$. Superoxide radicals are then formed by the reaction of the electrons with the O_2 adsorbed at the surface of TiO_2 particles, i.e., $e^- + O_2 \rightarrow \bullet O_2^-$. The holes react with water or hydroxyl groups to form hydroxyl radicals, i.e., $h^+ + H_2O \rightarrow \bullet OH + H^+$. [46]

For the superoxide radical ($\bullet O_2^-$), the peak height (h) in the 2-S0 sample is 2.2 $\times 10^5$. As $R_{S/Ti}$ increases, the peak height varies between 1.9 $\times 10^5$–2.5 $\times 10^5$. For the hydroxyl radical (•OH), the peak height varies in the range 1.6 $\times 10^6$–3.7 $\times 10^6$. The 2-S2 sample has the highest signal intensity for •OH and $\bullet O_2^-$. This indicates that the sample has the highest number of •OH and $\bullet O_2^-$, and is responsible for it having the highest pollutant degradation performance. The •OH and $\bullet O_2^-$ can degrade organic pollutants (MB) into non-toxic CO_2 and water, i.e., •OH or $\bullet O_2^-$ + organic pollutant $\rightarrow CO_2 + H_2O$.

Furthermore, as can be seen from Fig. 10, the •OH signal is stronger than the $\bullet O_2^-$ signal, indicating that more photo-generated holes (h^+) can transfer to the TiO_2 surface. For S-doped TiO_2, the outermost electronic orbitals of the S, O, and Ti elements are $3s^23p^4$, $2s^22p^4$, and $3d^24s^2$, respectively. When S^{2-} replaces O^{2-}, S^{2-} is neither a donor nor acceptor and has no influence on the carrier concentration in TiO_2. This is because S and O have the same number of outmost electrons. When the molar ratio of S/Ti is 2, S^{6+} begins to replace Ti^{4+} in the 2-S2 sample, resulting in the electron concentration becoming higher than the hole concentration. This is because S has more outer shell electrons than Ti. If the electrons and holes were both transferred to the surface of the TiO_2 particles, the $\bullet O_2^-$ signal would be stronger than the •OH signal; however, this was not the case, which could be due to a lot of the electrons being trapped by impurities or defect.

4. Conclusions

S doped (001)-TiO_2 with different $R_{S/Ti}$ were synthesized through the vapor-thermal method at 180 °C and 250 °C, respectively and systematically characterized by XRD, TEM, FT-IR, XPS, UV-Vis DRS, PL, BET, and ESR.

The S-doped sample at 180 °C displays little change in the structure, morphology, chemical state, and photocatalytic properties of TiO_2, indicating that the temperature was not high enough to achieve S doping. The effects of S-doping at 250 °C are as follows: (1) S-doping induces a crystal lattice distortion, and the ratio of the lattice parameters c/a varies with the $R_{S/Ti}$ ratios, reaching a maximum at $R_{S/Ti} = 3$. This is due to the difference in the ionic radius between S and the O and Ti it replaces. (2) S-doping changes the morphology of the particles and results in the aggregation of particles; consequently, the specific surface area decrease. (3) S-doping increases the adsorption coefficient A_e from 0.9% to 68.5% due to the increase of oxygen vacancies and SO_4^{2-} on the surface of the TiO_2 particles. (4) S-doping increases the degradation rate from 6.9×10^{-2} min^{-1} to 18.2×10^{-2} min^{-1}. This is due to the presence of more •OH and $•O^{2-}$ radicals with high reactivity.

Acknowledgments

A portion of this work was performed on the Steady High Magnetic Field Facilities, High Magnetic Field Laboratory, CAS. This work was supported by the open fund for Discipline Construction, Institute of Physical Science and Information Technology, Anhui University; National Natural Science Foundation of China (Grant Nos. 51471001).

References

[1] H. Hussain, G. Tocci, T. Woolcot. Structure of a model TiO_2 photocatalytic interface. Nature. Mat., 2017, 16(4): 461.

[2] S. Selcuk, A. Selloni. Facet-dependent trapping and dynamics of excess electrons at anatase TiO_2 surfaces and aqueous interfaces. Nature. Mat., 2016, 15(10): 1107.

[3] A. Omri, S. D. Lambert, J. Geens, F. Bennour, M. Benzinal. Synthesis, surface characterization and photocatalytic activity of TiO_2 supported on almond shell activated carbon. J. Mater. Sci. Tech., 2014, 30: 894-902.

[4] B. Cao, G. Li, H. Li. Hollow spherical RuO_2@TiO_2@Pt bifunctional photocatalyst for coupled H_2 production and pollutant degradation. Appl. Catal. B., 2016, 194: 42-49.

[5] G. Liu, H. G. Yang, J. Pan, Y. Q. Yang, G. Q. Lu, H. M. Cheng, Titanium dioxide crystals with tailored facets. Chem. Rev. 2014(114): 9559-9612

[6] S. W. Liu, J. G. Yu, M. Jaroniec, Tunable photocatalytic selectivity of hollow TiO_2 microspheres composed of anatase polyhedra with exposed {001} facets. J. Am. Chem. Soc. 2010(132): 11914-11916.

[7] O. Arutanti, A. B. D. Nandiyanto, T. Ogi, F. Iskandar, T. O. Kim, K. Okuyama, Synthesis of composite WO_3/TiO_2 nanoparticles by flame-assisted spray pyrolysis and their photocatalytic activity. J. Alloy. Compd. 591 (2014) 121-126.

[8] J. G. Yu, J. X. Low, W. Xiao. Enhanced Photocatalytic CO_2- Reduction Activity of Anatase TiO_2 by Coexposed {001} and {101} Facets. J. Am. Chem. Soc. 2014(136): 8839-8842.

[9] X. G. Liu, G. J. Dong, S. P. Li. Direct Observation of Charge Separation on Anatase TiO_2 Crystals with Selectively Etched {001} Facets. J. Am. Chem. Soc. 2016(138): 2917-2920.

[10] Y. Wang, H. Sun, S. Tan, et al. Role of point defects on the reactivity of reconstructed anatase titanium dioxide (001) surface. Nat. Commun., 2013, 4: 2214.

[11] X. Chen, C. Burda. The electronic origin of the visible-light absorption properties of C-, N-and S-doped TiO_2 nanomaterials. J. Am. Chem. Soc., 2008, 130(15): 5018-5019.

[12] B. Li, Z. Zhao, F. Gao, et al. Mesoporous microspheres composed of carbon-coated TiO_2 nanocrystals with exposed {001} facets for improved visible light photocatalytic activity. Appl. Catal. B., 2014, 147: 958-964.

[13] L. Chen, X. Zhou, B. Jin, et al. Heterojunctions in g-C_3N_4/B-TiO_2 nanosheets with exposed {001} plane and enhanced visible-light photocatalytic activities. Int. J. Hydrogen. Energ., 2016, 41(18): 7292-7300.

[14] L. Cao, R. Wang, D. Wang, et al. Enhanced visible light photocatalytic activity for the hybrid MoS_2/anatase TiO_2 (001) nanocomposite: A first-principles study. Chem. Phys. Lett., 2014, 612: 285-288.

[15] H. Shi, S. Zhang, X. Zhu, et al. Uniform gold-nanoparticle-decorated {001}-faceted anatase TiO_2 nanosheets for enhanced solar-light photocatalytic reactions. ACS. Appl. Mater. Inter., 2017, 9(42): 36907-36916.

[16] J. Yan, G. Wu, W. Dai, et al. Synthetic design of gold nanoparticles on anatase TiO_2 {001} for enhanced visible light harvesting. ACS. Sustain. Chem. Eng., 2014, 2(8): 1940-1946.

[17] P. Zhou, J. Wu, W. Yu, et al. Vectorial doping-promoting charge transfer in anatase TiO_2 {001} surface. Appl. Surf. Sci., 2014, 319: 167-172.

[18] F. Wang, P. P. Ban, J. P. Parry, et al. Enhanced photocatalytic properties of N–P co-doped TiO_2 nanosheets with {001} facets. Rare Metals, 2016, 35(12): 940-947.

[19] C. Han, M. Pelaez, V. Likodimos, et al. Innovative visible light-activated sulfur doped TiO_2 films for water treatment. Appl. Catal. B., 2011, 107(1-2): 77-87.

[20] T. Ohno, T. Mitsui, M. Matsumura. Photocatalytic activity of S-doped TiO_2 photocatalyst under visible light. Chem. Lett., 2003, 32(4): 364-365.

[21] T. Ohno, M. Akiyoshi, T. Umebayashi, et al. Preparation of S-doped TiO_2 photocatalysts and their photocatalytic activities under visible light. Appl. Catal. A-Gen., 2004, 265(1): 115-121.

[22] T. Ohno. Preparation of visible light active S-doped TiO_2 photocatalysts and their photocatalytic activities. Water. Sci. Technol., 2004, 49(4): 159-163.

[23] P. Ramacharyulu, J. P. Kumar, G. K. Prasad, et al. Sulphur doped nano TiO_2: synthesis, characterization and photocatalytic degradation of a toxic chemical in presence of sunlight. Mater. Chem. Phys., 2014, 148(3): 692-698.

[24] G. Colón, M. C. Hidalgo, G. Munuera, et al. Structural and surface approach to the enhanced photocatalytic activity of sulfated TiO_2 photocatalyst. Appl. Catal. B., 2006, 63(1-2): 45-59.

[25] C. T. Dinh, T. D. Nguyen, F. Kleitz, et al. Shape-controlled synthesis of highly crystalline titania nanocrystals. ACS nano, 2009, 3(11): 3737-3743.

[26] T. R. Gordon, M. Cargnello, T. Paik, et al. Nonaqueous synthesis of TiO_2 nanocrystals using TiF_4 to engineer morphology, oxygen vacancy concentration, and photocatalytic activity. J. Am. Chem. Soc., 2012, 134(15): 6751-6761.

[27] H. Wang, S. Cao, Z. Fang, et al. CeO_2 doped anatase TiO_2 with exposed (001) high energy facets and its performance in selective catalytic reduction of NO by NH_3. Appl. Surf. Sci., 2015, 330: 245-252.

[28] G. Zhang, Y. C. Zhang, M. Nadagouda, et al. Visible light-sensitized S, N and C co-doped polymorphic TiO2 for photocatalytic destruction of microcystin-LR. Appl. Catal. B., 2014, 144: 614-621.

[29] S. M. Jung, P. Grange. Characterization and reactivity of pure TiO_2–SO_4^{2-} SCR catalyst: influence of SO_4^{2-} content. Catal. Today., 2000, 59(3-4): 305-312.

[30] M. Schwanninger, J. C. Rodrigues, H. Pereira, et al. Effects of short-time vibratory ball milling on the shape of FT-IR spectra of wood and cellulose. Vib. Spectrosc., 2004, 36(1): 23-40.

[31] A. S. Sivam, D. Sun-Waterhouse, C. O. Perera, et al. Application of FT-IR and Raman spectroscopy for the study of biopolymers in breads fortified with fibre and polyphenols. Food. Res. Int., 2013, 50(2): 574-585.

[32] M. Shi, J. Shen, H. Ma, et al. Preparation of graphene–TiO2 composite by hydrothermal method from peroxotitanium acid and its photocatalytic properties. Colloid. Surface. A., 2012, 405: 30-37.

[33] A. Ramadoss, S. J. Kim. Improved activity of a graphene–TiO2 hybrid electrode in an electrochemical supercapacitor. Carbon, 2013, 63: 434-445.

[34] Z. G. Chen, L. Zhu, J. X. Xia, et al. Synthesis of flower-like Pd/BiOCl composites via reactable ionic liquid and their enhanced photocatalytic properties. Mater. Technol., 2014, 29(4): 245-251.

[35] P. L. Anto, R. J. Anto, H. T. Varghese, et al. FT- IR, FT- Raman and SERS spectra of anilinium sulfate. J. Raman. Spectrosc., 2009, 40(12): 1810-1815.

[36] M. Thomas, H. H. Richardson. Two-dimensional FT-IR correlation analysis of the phase transitions in a liquid crystal, 4′-n-octyl-4-cyanobiphenyl (8CB). Vib. Spectrosc., 2000, 24(1): 137-146.

[37] X. Pan, Y. Zhao, S. Liu, et al. Comparing graphene-TiO_2 nanowire and graphene-TiO_2 nanoparticle composite photocatalysts. ACS. Appl. Mater. Inter., 2012, 4(8): 3944-3950.

[38] L. Wang, M. Wen, W. Wang, et al. Photocatalytic degradation of organic pollutants using rGO supported TiO_2-CdS composite under visible light irradiation. J. Alloy. Compd., 2016, 683: 318-328.

[39] J. M. Song, C. J. Mao, H. L. Niu, et al. Hierarchical structured bismuth oxychlorides: self-assembly from nanoplates to nanoflowers via a solvothermal route and their photocatalytic properties. CrystEngComm, 2010, 12(11): 3875-3881.

[40] S. Weng, J. Hu, M. Lu, et al. In situ photogenerated defects on surface-complex BiOCl (010) with high visible-light photocatalytic activity: A probe to disclose the charge transfer in BiOCl (010)/surface-complex system. Appl. Catal. B., 2015, 163: 205-213.

[41] P. Periyat, S. C. Pillai, D. E. McCormack, et al. Improved high-temperature stability and sun-light-driven photocatalytic activity of sulfur-doped anatase TiO_2. J. Phys. Chem. C., 2008, 112(20): 7644-7652.

[42] M. Sun, Y. Wang, Y. Fang, et al. Construction of MoS_2/CdS/TiO_2 ternary composites with enhanced photocatalytic activity and stability. J. Alloy. Compd., 2016, 684: 335-341.

[43] C. Liu, X. Zhu, P. Wang, et al. Defects and interface states related photocatalytic properties in reduced and subsequently nitridized Fe_3O_4/TiO_2. J. Mater. Sci. Technol., 2018, 34(6): 931-941.

[44] F. Ning, M. Shao, S. Xu, et al. TiO_2/graphene/NiFe-layered double hydroxide nanorod array photoanodes for efficient photoelectrochemical water splitting. Energ. Environ. Sci., 2016, 9(8): 2633-2643.

[45] D. Zhao, G. Sheng, C. Chen, et al. Enhanced photocatalytic degradation of methylene blue under visible irradiation on graphene@ TiO_2 dyade structure. Appl. Catal. B., 2012, 111: 303-308.

[46] M. Wang, Y. Q. Ma, X. Sun, et al. Building of $CoFe_2/CoFe_2O_4$/MgO architectures: Structure, magnetism and surface functionalized by TiO_2. Appl. Surf. Sci., 2017, 392: 1078-1087.

[47] M. Mouanga, P. Bercot. Electrochemical analysis of thiourea on platinum in non-aqueous electrolyte. Int. J. Electrochem. Sci, 2011, 6: 1007-1013.

[48] T. Umebayashi, T. Yamaki, H. Itoh, et al. Band gap narrowing of titanium dioxide by sulfur doping. Appl. Phys. Lett., 2002, 81(3): 454-456.

[49] S. Sahu, P. Rani Sahoo, S. Patel, et al. Oxidation of thiourea and substituted thioureas: a review. J. Sulfur. Chem., 2011, 32(2): 171-197.

[50] F. Wei, L. Ni, P. Cui. Preparation and characterization of N–S-codoped TiO_2 photocatalyst and its photocatalytic activity. J. Hazard. Mater., 2008, 156(1-3): 135-140.

[51] X. Chen, L. Liu, Y. Y. Peter, et al. Increasing solar absorption for photocatalysis with black hydrogenated titanium dioxide nanocrystals. Science, 2011, 331(6018): 746-750.

[52] H. Li, J. Shang, H. Zhu, et al. Oxygen vacancy structure associated photocatalytic water oxidation of BiOCl. ACS Catal., 2016, 6(12): 8276-8285.

[53] X. Wang, C. Y. Jimmy, P. Liu, et al. Probing of photocatalytic surface sites on SO_4^{2-}/TiO_2 solid acids by in situ FT-IR spectroscopy and pyridine adsorption. J. Photoch. Photobio. A., 2006, 179(3): 339-347.

[54] H. Tang, H. Berger, P. E. Schmid, et al. Photoluminescence in TiO_2 anatase single

crystals. Solid. State. Commun., 1993, 87(9): 847-850.

[55] H. Tang, K. Prasad, R. Sanjines, et al. Electrical and optical properties of TiO_2 anatase thin films. J. Appl. Phys., 1994, 75(4): 2042-2047.

Table and Figure captions

Table 1 The unit cell parameters *a*, *c* and the *c*/*a* value for S-doped (001)-TiO_2 at 250 °C.

Table 2 Wavenumber at the absorbance peak and the corresponding vibration mode.

Table 3 The chemical states (CS) of Ti and O and their corresponding binding energies (BE) and ratios for 1-S0, 1-S2, and 1-S5.

Table 4 The chemical states (CS) of Ti, O, and S elements and their corresponding binding energies (BE) and ratios for 2-S0, 2-S0.5, 2-S1, 2-S2, 2-S3, 2-S4, and 2-S5.

Table 5 The values of the adsorption efficiency (A_e), degradation efficiency (D_e), and the apparent reaction rate constant K_{app} for the 180 ℃ samples.

Table 6 The values of the adsorption efficiency (A_e), degradation efficiency (D_e), and the apparent reaction rate constant K_{app} for the 250 ℃ samples.

Table 7 Textural parameters of all samples.

Fig. 1 Experimental (×) and calculated (—) X-ray powder diffraction patterns of 1-S0 (a) and 2-S2 (b). Peak positions are shown as small markers (|). The lower trace represents the difference between the calculated and experimental data.

Fig. 2 TEM images (a, b, and c) and HRTEM images (d, e, and f) for 1-S0, 2-S0, and 2-S2.

Fig. 3 The FT-IR spectra of 1-S0, 1-S2, and 1-S5 (a); 2-S0, 2-S2, and 2-S5 (b).

Fig. 4 Core level XPS spectra of Ti 2p (a) and O 1s (b) for 1-S2. The solid line is the experimental curve, the dashed line is the fitted curve, and the open circles are the sum of the fitted curves.

Fig. 5 Core level XPS spectra of Ti 2p (a and d), O 1s (b and e), and S 2p (c and f) for 2-S1 and 2-S3. The solid line is the experimental curve, the dashed line is the fitted curve, and the open circles are the sum of the fitted curves.

Fig. 6 Valence-band XPS spectra (a) and the UV-Vis DRS (b) of 2-S0, 2-S0.5, 2-S1, 2-S3, and 2-S5. The inset in (b) is the magnified plot of UV-Vis DRS in the visible light region.

Fig. 7 Variation of methylene blue concentration C/C_0 with time in the presence of 1-S0–1-S5 (a) and 2-S0–2-S5 (b) under the radiation of the xenon lamp.

Fig. 8 Nitrogen adsorption-desorption isotherms for 1-S0, 1-S2, and 1-S5 (a) and 2-S0, 2-S, and 2-S5 (b) samples. The insets show the pore size distribution calculated using the BJH method.

Fig. 9 The PL spectra with an excitation wavelength λ_{ex} = 300 nm for 1-S0, 1-S0.5, 1-S2, 1-S3, and 1-S5 (a) and 2-S0, 2-S0.5, 2-S2, 2-S3, and 2-S5 (b).

Fig. 10 ESR spectra of radical adducts trapped by DMPO in 2-S0 (a, e), 2-S2 (b, f), 2-S3 (c, g), and 2-S2 (d, h) dispersions: (a, b, c, d) DMPO-•OH formed in aqueous dispersions, (e, f, g, h) DMPO-•O_2^- formed in methanol dispersion.

Tables and Figures

Table 1

	2-S0	2-S0.5	2-S1	2-S2	2-S3	2-S4	2-S5
a (Å)	3.7852	3.7876	3.7867	3.7866	3.7860	3.7864	3.7859
c (Å)	9.5139	9.5120	9.5091	9.5137	9.5131	9.5069	9.5083
c/a	2.5135	2.5114	2.5118	2.5125	2.5127	2.5108	2.5115

Table 2

Wavenumber (cm^{-1})	Vibration mode	References
425-840	Ti-O or Ti-O-Ti	[37,38]
880	alkoxy C-OH stretching vibrations	[32,33]
1060	Ti-S	[28]
1160	Ti-O-S	[19]
1400	The S=O stretching vibration	[29]
1800,2515	The C=O and O-H stretching vibration of -COOH in organic residues	[30,31]
1633,3400	The flexural vibrations of O-H in free water molecules	[39,40]
2850,2920	The C-H stretching vibration	[34]
2138	The C-N stretching vibration	[35,36]

Table 3

180℃		Ti		O	
	CS	TiO_2	TiO_x	TiO_2	-OH
1-S0	BE（eV）	458.9	460.2	530.1	531.3
	Ratio (%)	97.9	2.1	82.1	17.9
1-S2	BE（eV）	458.9	460.2	530.1	531.2
	Ratio (%)	98.5	1.5	79.2	20.8
1-S5	BE（eV）	458.8	460.2	530.0	531.1
	Ratio (%)	98.6	1.4	78.3	21.7

Table 4

250℃		Ti		O			S		
	CS	TiO_2	TiO_x	TiO_2	-OH	O_v	Ti-S	S	S^{+6}
2-S0	BE（eV）	458.8	460.2	530.0	531.0	532.7	\	\	\
	Ratio (%)	98.5	1.5	80.6	15.1	4.3	\	\	\
2-S0.5	BE（eV）	458.9	460.2	530.1	530.9	532.4	\	\	\
	Ratio (%)	97.2	2.8	74.5	15.6	9.9	\	\	\
2-S1	BE（eV）	458.8	460.2	530.0	530.8	532.2	163.5	164.4	\
	Ratio (%)	96.6	3.4	69.7	12.8	17.5	49.5	50.5	\
2-S2	BE（eV）	458.9	460.2	530.1	530.8	532.4	163.5	164.4	168.0
	Ratio (%)	97.6	2.4	61.7	19.4	18.9	38.7	22.8	38.5
2-S3	BE（eV）	458.9	460.2	530.2	531.0	532.2	163.5	164.4	168.0
	Ratio (%)	96.9	3.1	71.7	5.4	22.9	50.8	23.5	25.7
2-S4	BE（eV）	458.9	460.2	530.1	530.9	532.3	163.5	164.4	168.0
	Ratio (%)	97.6	2.4	68.7	9.7	21.6	42.6	35.0	22.4
2-S5	BE（eV）	458.8	460.2	530.0	530.9	532.3	163.5	164.4	168.0
	Ratio (%)	97.7	2.3	68.5	11.6	19.9	48.4	37.3	14.3

Table 5

Samples	1-S0	1-S0.5	1-S1	1-S2	1-S3	1-S4	1-S5
K_{app} (10^{-2} min^{-1})	1.7	1.5	1.8	1.9	3.5	3.7	3.5
A_e (%)	1.9	0	0	0	0.7	5.7	1.0
D_e (%) (t = 120 min)	98.4	92.5	95.6	97.8	99.8	99.8	99.8

Table 6

Samples	2-S0	2-S0.5	2-S1	2-S2	2-S3	2-S4	2-S5
K_{app} (10^{-2} min^{-1})	6.9	5.5	11.7	18.2	6.2	12.1	17.6
A_e (%)	0.9	14.1	35.1	56.9	56.3	54.8	68.5
D_e (%) (t = 80 min)	99.8	99.4	99.5	99.8	99.6	99.4	99.7

Table 7

Samples	1-S0	1-S0.5	1-S1	1-S2	1-S3	1-S4	1-S5
$S_{BET}(m^2g^{-1})$	174.8	128.8	210.9	128.2	98.4	109.8	145.9
D_p(nm)	8.29	13.9	9.14	11.9	14.5	14.4	11.6
Samples	2-S0	2-S0.5	2-S1	2-S2	2-S3	2-S4	2-S5
$S_{BET}(m^2g^{-1})$	98.6	123.6	81.7	92.1	120.8	89.9	89.6
D_p(nm)	15.0	13.6	18.4	18.0	14.8	17.8	19.1

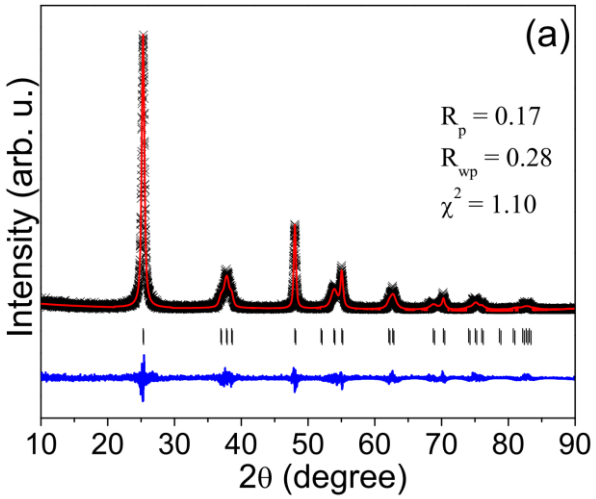

Fig. 1(a) X.Y. Sun et al.

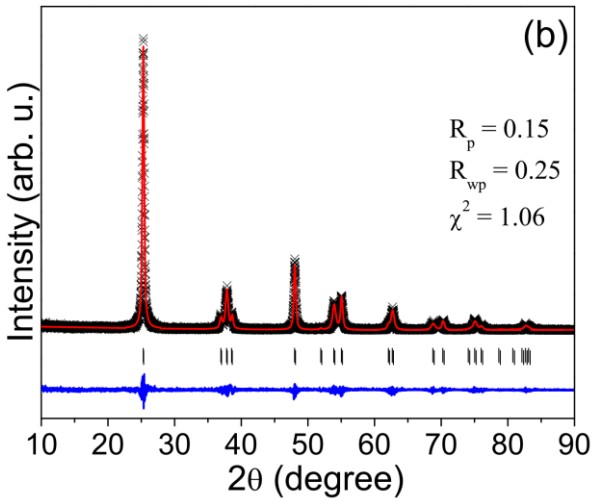

Fig. 1(b) X.Y. Sun et al.

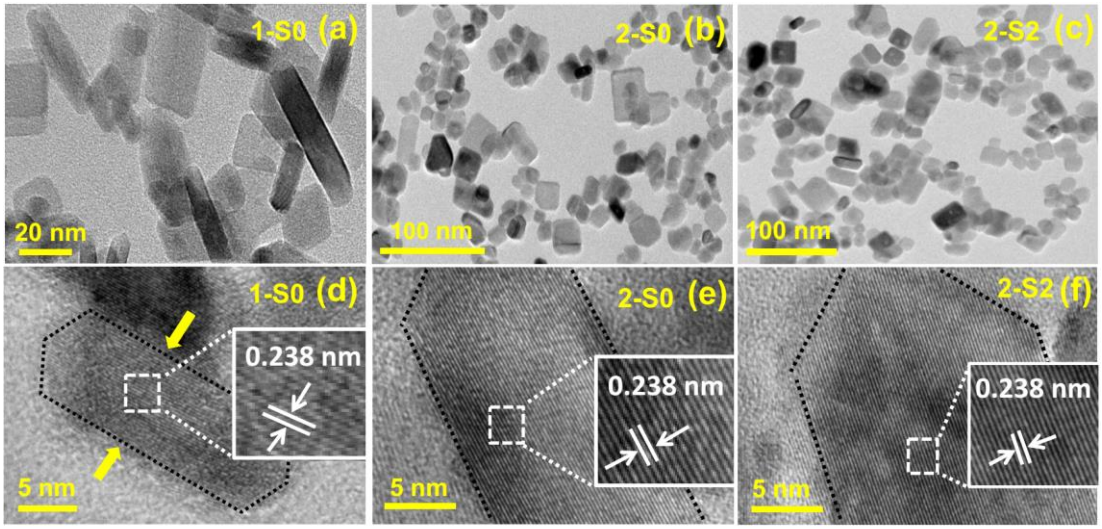

Fig. 2 X.Y. Sun et al.

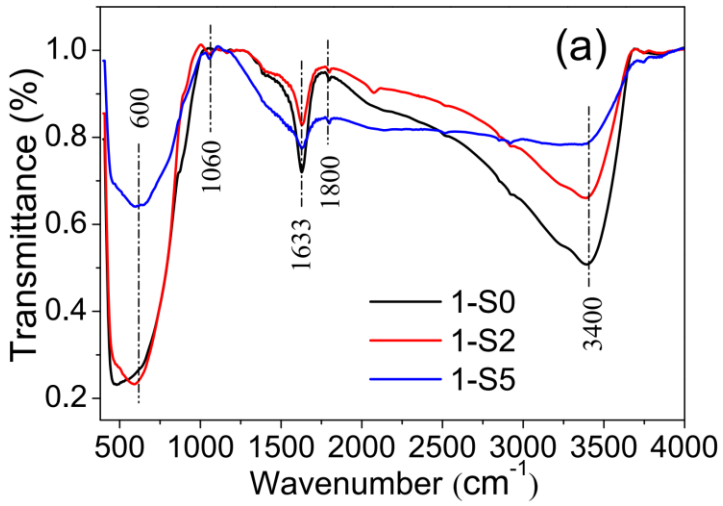

Fig. 3(a) X.Y. Sun et al.

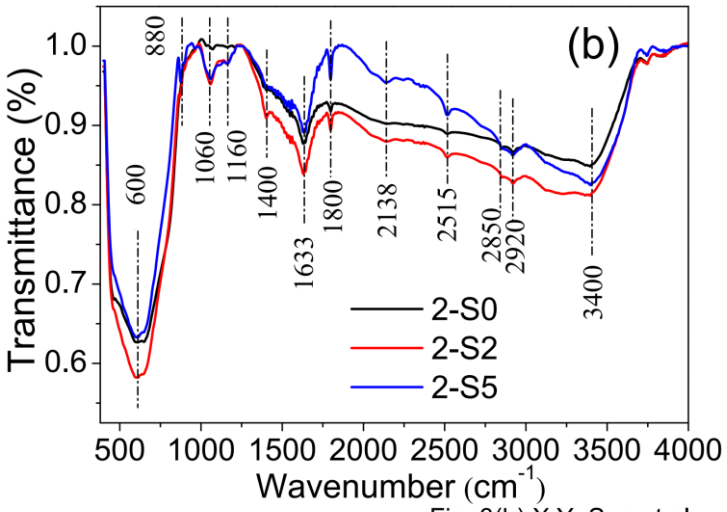

Fig. 3(b) X.Y. Sun et al.

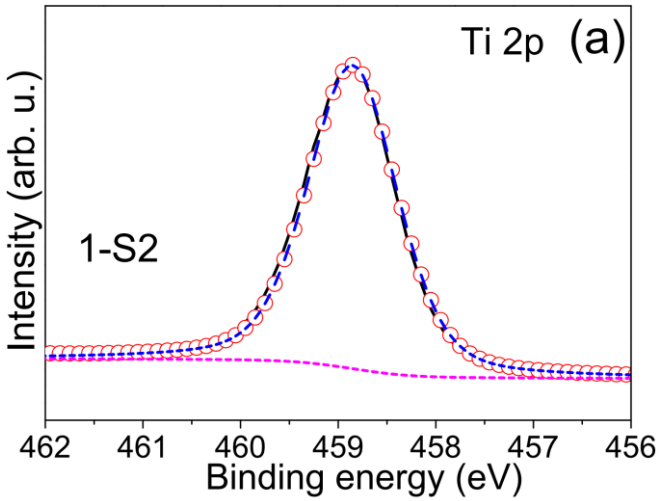

Fig. 4(a) X.Y. Sun et al.

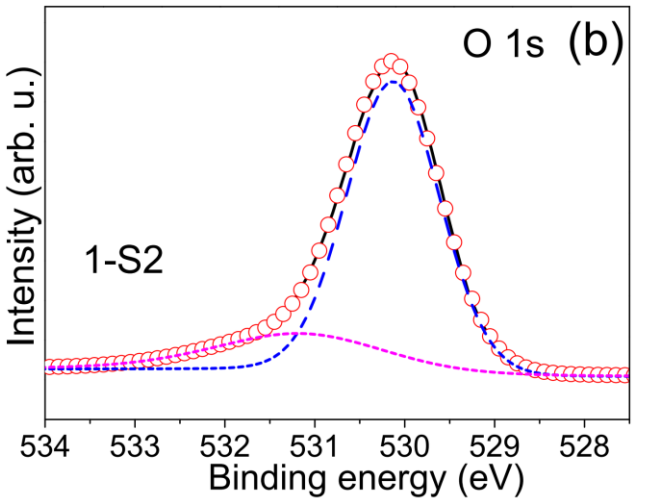

Fig. 4(b) X.Y. Sun et al.

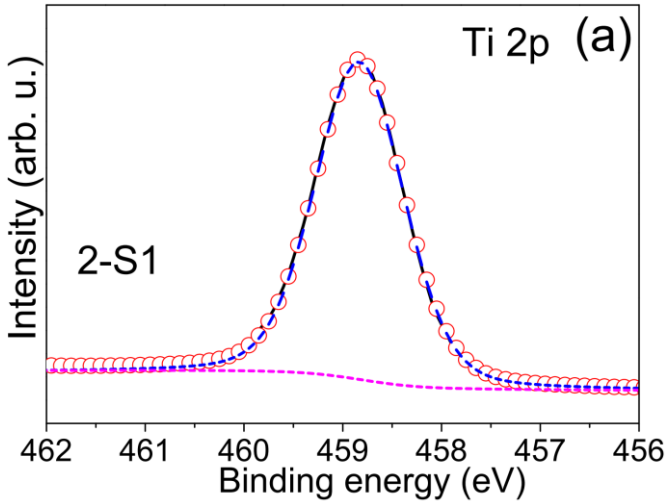

Fig. 5(a) X.Y. Sun et al.

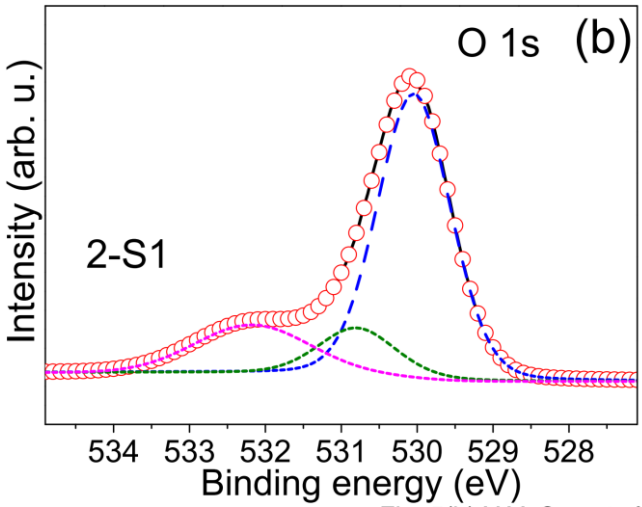

Fig. 5(b) X.Y. Sun et al.

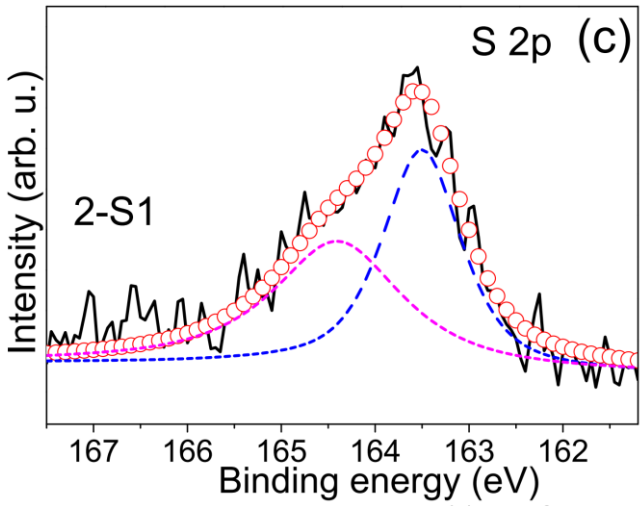

Fig. 5(c) X.Y. Sun et al.

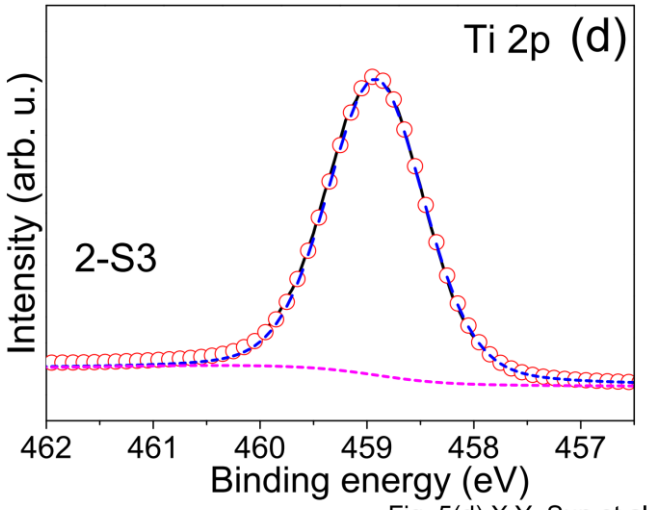

Fig. 5(d) X.Y. Sun et al.

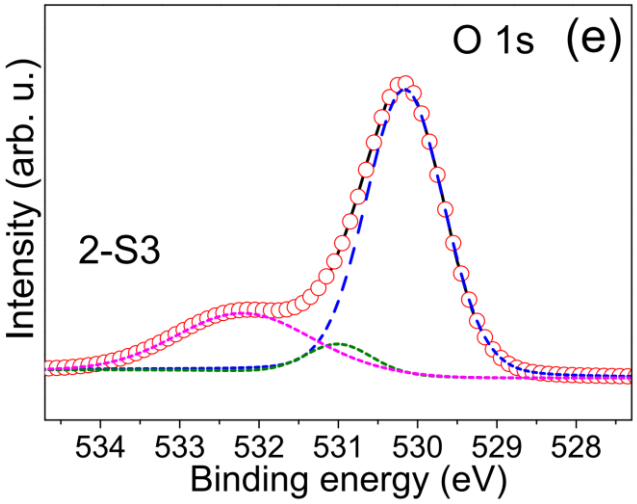

Fig. 5(e) X.Y. Sun et al.

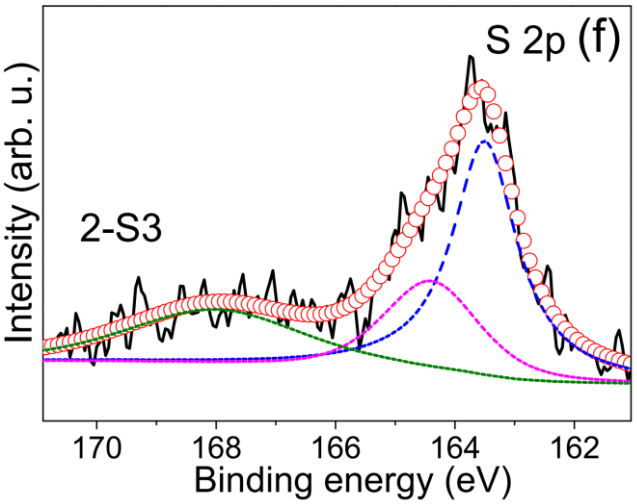

Fig. 5(f) X.Y. Sun et al.

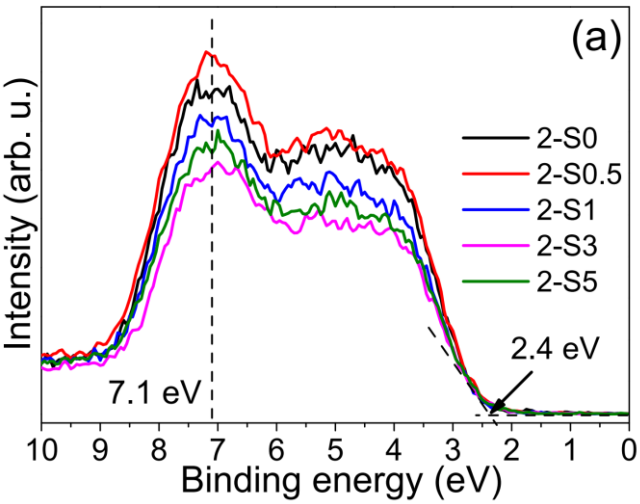

Fig. 6(a) X.Y. Sun et al.

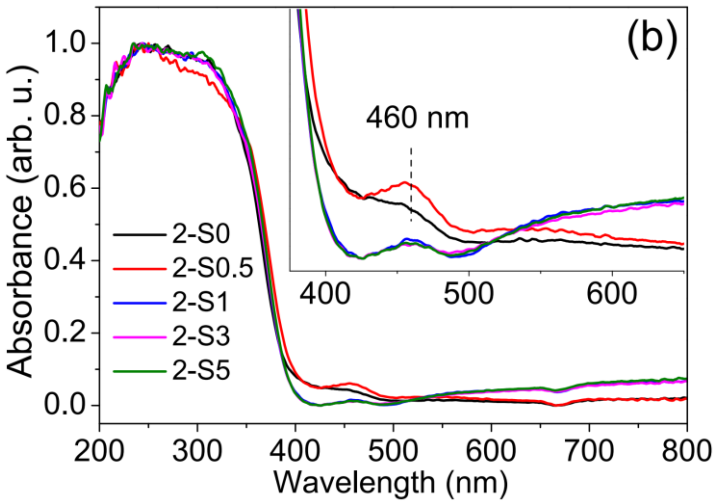

Fig. 6(b) X.Y. Sun et al.

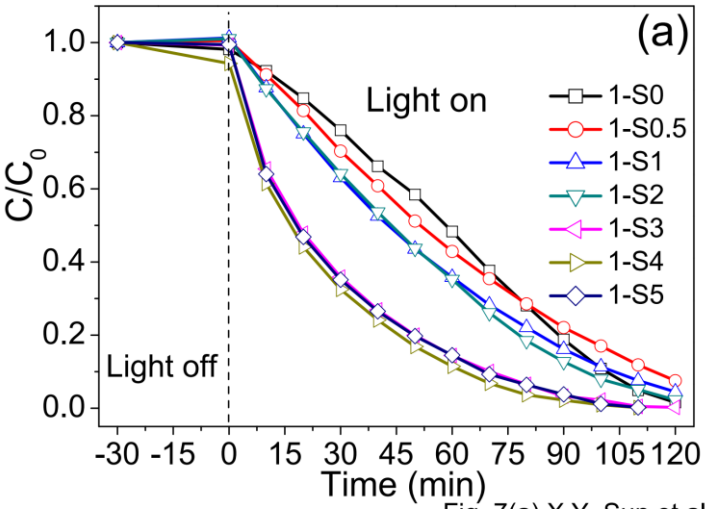

Fig. 7(a) X.Y. Sun et al.

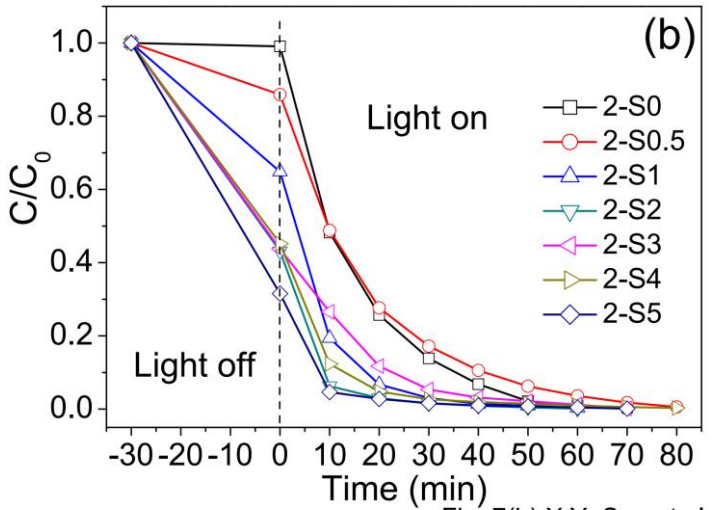

Fig. 7(b) X.Y. Sun et al.

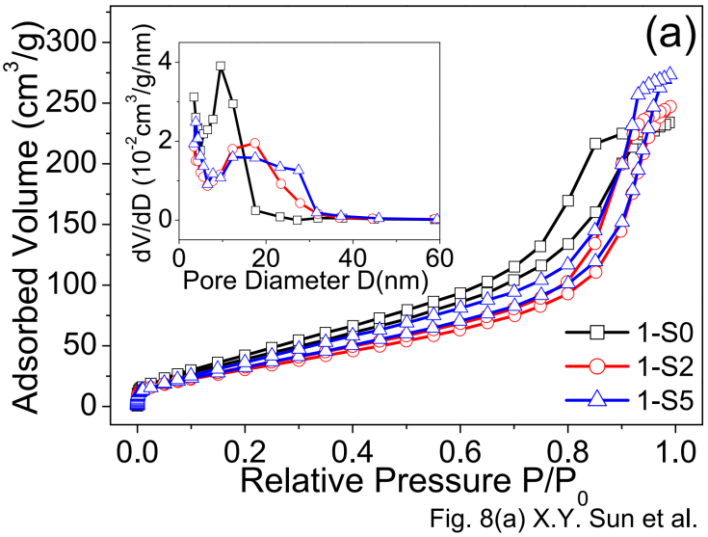

Fig. 8(a) X.Y. Sun et al.

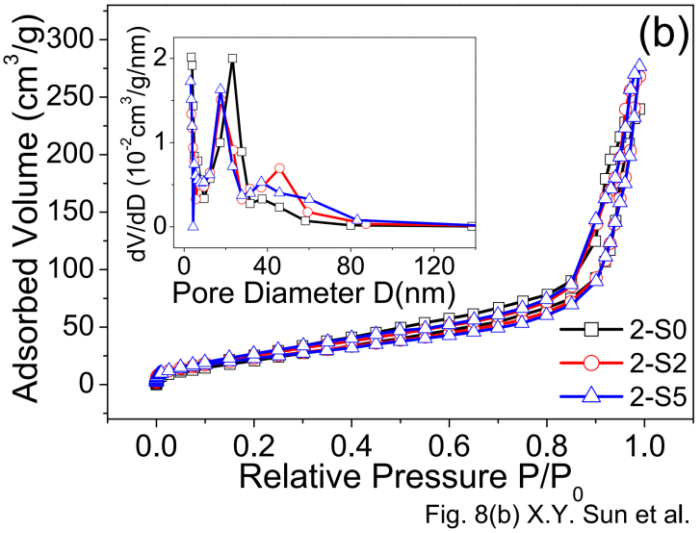

Fig. 8(b) X.Y. Sun et al.

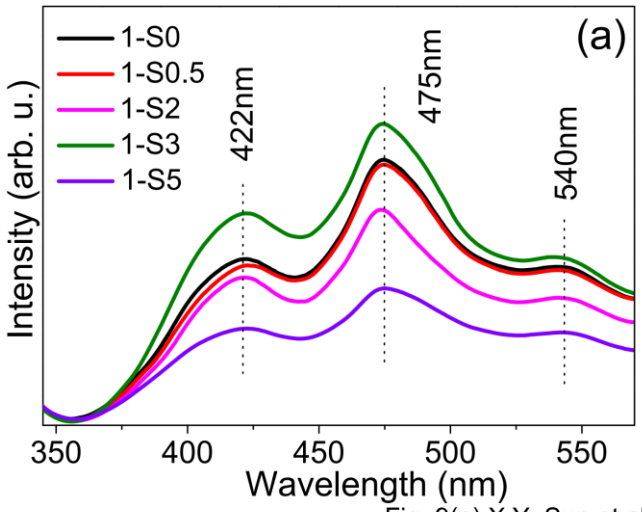

Fig. 9(a) X.Y. Sun et al.

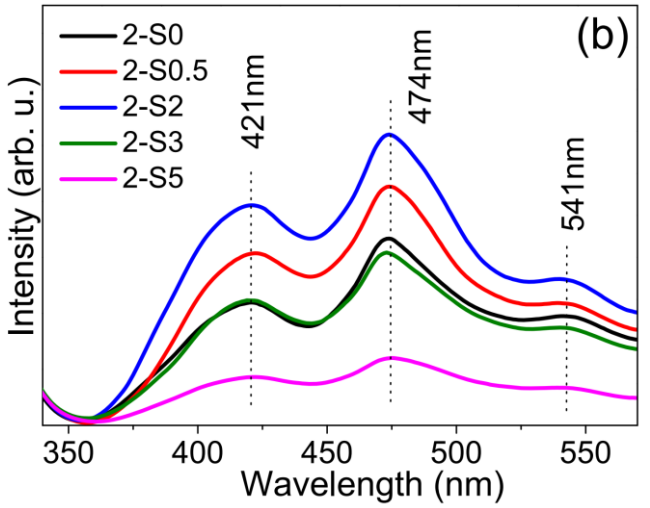

Fig. 9(b) X.Y. Sun et al.

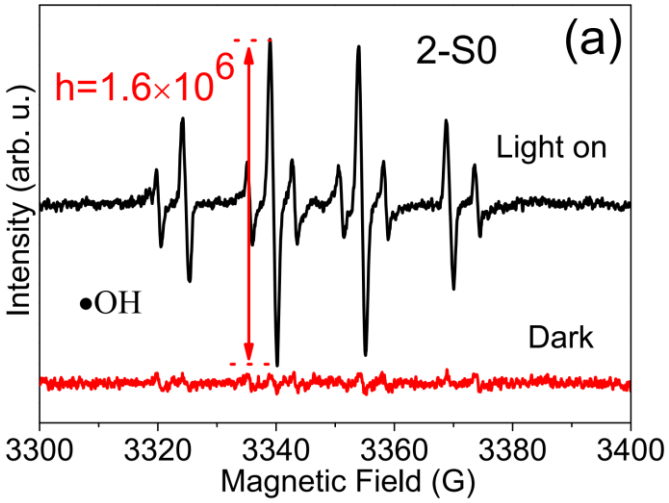

Fig. 10(a) X.Y. Sun et al.

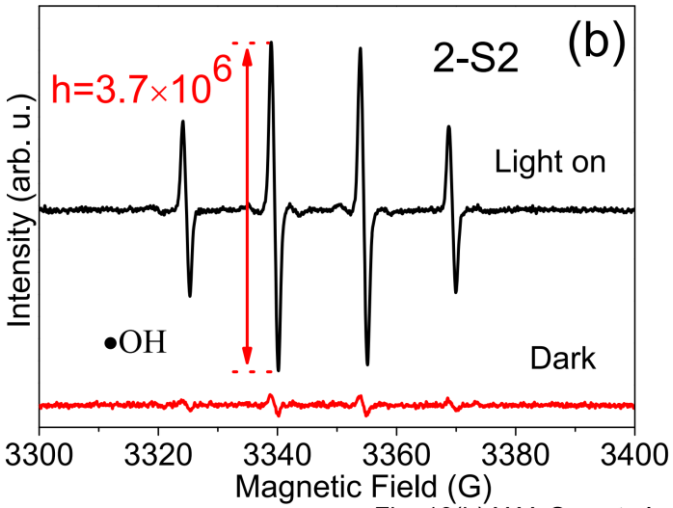

Fig. 10(b) X.Y. Sun et al.

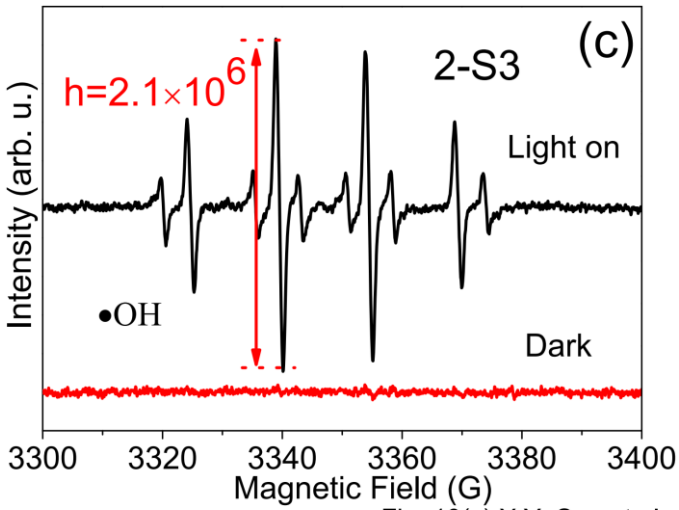

Fig. 10(c) X.Y. Sun et al.

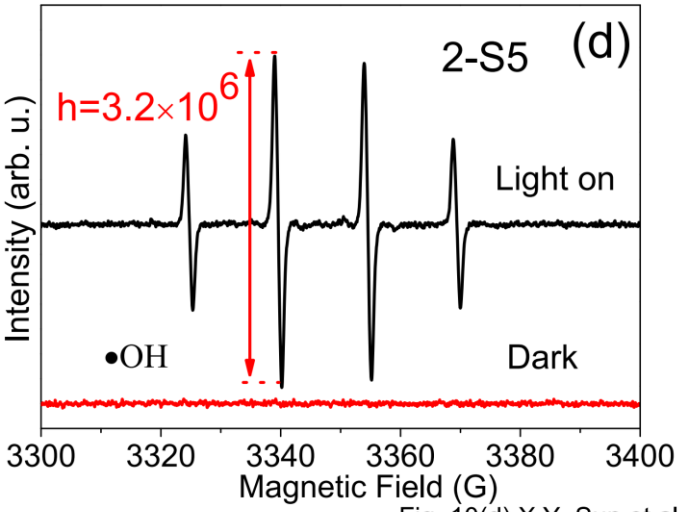

Fig. 10(d) X.Y. Sun et al.

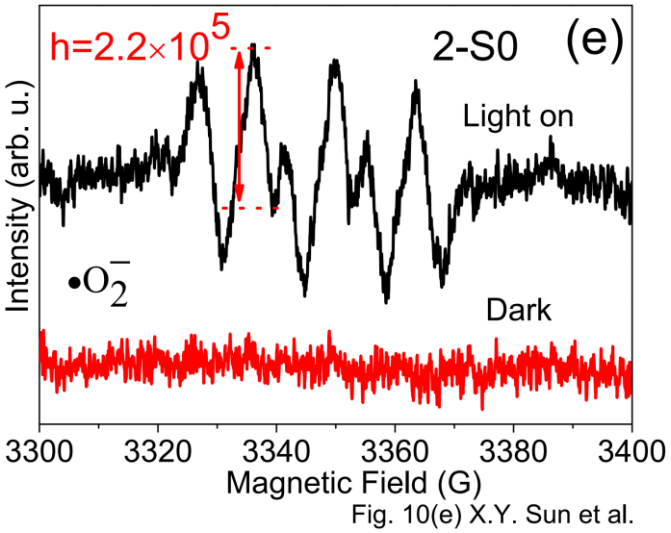

Fig. 10(e) X.Y. Sun et al.

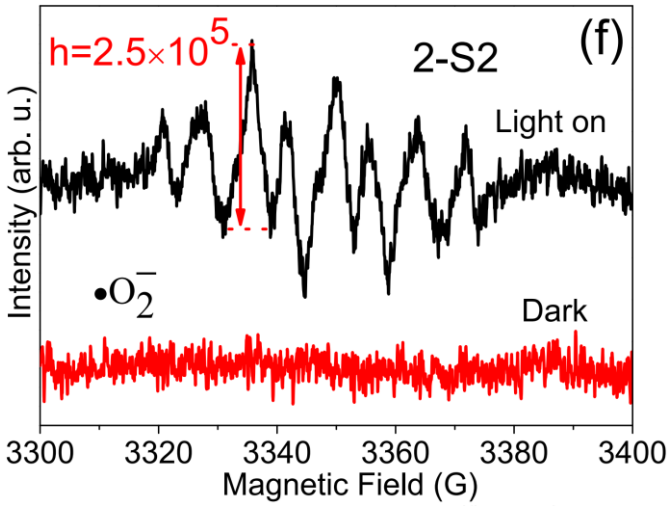

Fig. 10(f) X.Y. Sun et al.

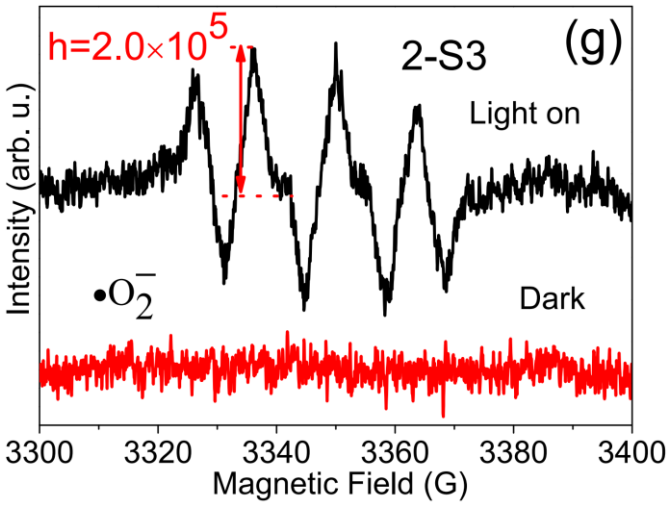

Fig. 10(g) X.Y. Sun et al.

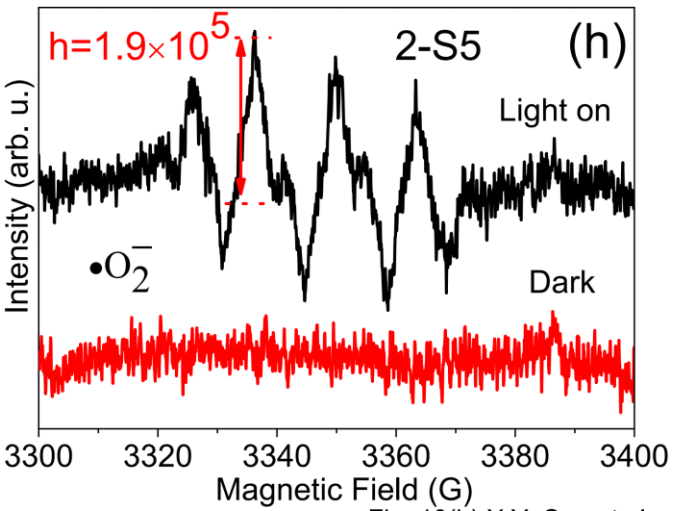

Fig. 10(h) X.Y. Sun et al.